Ab initio study of low-energy collective electronic excitations in bulk Pb

X. Zubizarreta,[1,2] V. M. Silkin,[1,2,3] and E. V. Chulkov[1,2,4]

[1]*Donostia International Physics Center (DIPC), Paseo de Manuel Lardizabal 4, 20018 San Sebastián/Donostia, Basque Country, Spain*

[2]*Departamento de Física de Materiales, Facultad de Ciencias Químicas, Universidad del País Vasco/Euskal Herriko Unibertsitatea, Apdo. 1072, 20080 San Sebastián/Donostia, Basque Country, Spain*

[3]*IKERBASQUE, Basque Foundation for Science, 48011 Bilbao, Spain*

[4]*Centro de Física de Materiales CFM–Materials Physics Center MPC, Centro Mixto CSIC-UPV/EHU, Paseo de Manuel Lardizabal 5, 20018 San Sebastián/Donostia, Basque Country, Spain*

(Received 1 October 2012; revised manuscript received 27 January 2013; published 8 March 2013)

A theoretical study of the dynamical dielectric response of bulk lead at low energies is presented. The calculations are performed with full inclusion of the electronic band structure calculated by means of a first-principles pseudopotential approach. The effect of inclusion of the spin-orbit interaction in the band structure on the excitation spectra in Pb is analyzed, together with dynamical exchange-correlation and local-field effects. In general, results show significant anisotropy effects on the dielectric response of bulk Pb. At small momentum transfers along three different high-symmetry directions, the calculated excitation spectra present several peaks with strong acousticlike dispersion in the energy range below 2 eV. The analysis shows that only one of such modes existing at momentum transfers along the Γ–K direction can be interpreted as a true acousticlike plasmon, whereas all other modes are originated from the enhanced number of intraband electron-hole excitations at corresponding energies. Comparison with available optical experimental data shows good agreement.

DOI: 10.1103/PhysRevB.87.115112 PACS number(s): 71.20.Gj, 71.45.Gm

I. INTRODUCTION

In the last two decades, significant progress was achieved in the understanding of dynamical processes involving both single particles (electrons and holes) and collective electronic excitations in metallic systems from the so-called *ab initio* perspective. In particular, in the course of the study of dynamics of electronic excitations, the relative importance of such intrinsic processes as electron-phonon and electron-electron decay was thoroughly analyzed.[1,2] One of the important results of these investigations was the demonstration of a crucial role of the electronic band structure of real solids in such events.

At the same time, it is known that the band structure can be influenced by spin-orbit (SO) effects, especially in heavy elements. Remarkable examples are lead, bismuth, and bismuth tellurohalides, where the SO interaction produces strong modifications of the band structure[3–5] and vibrational spectra,[6–8] influencing the electron-phonon interaction in these materials.

The effect of the SO interaction on the electronic structure was intensively investigated in the past, while the inclusion of this interaction into calculation of dielectric properties from first principles was performed in few cases only. Thus, it was demonstrated that the SO interaction induces sizable effects in the optical properties and dielectric properties in the small-momentum-transfer limit of heavy elements, in particular Pb.[9] However, a detailed study of the impact of the SO interaction on the excitation spectrum of Pb over a whole momentum-energy domain is still missing, especially in a low-energy region where the major effect is expected. This constitutes a main topic of this study, in such a way giving a whole picture of the low-energy electronic dynamics in the elemental lead in addition to the phonon dynamics studied heavily up to now.

One of the characteristics of lead is that it presents the second-highest critical temperature of all bulk elemental superconductors ($T_c = 7.23$ K),[10] which has been shown to be related to its large electron-phonon coupling (EPC) constant. In addition, SO coupling has a strong impact on the electron-phonon interaction in bulk Pb, increasing its strength as much as 44%.[6] Studying the electronic collective excitations near the Fermi level (E_F) and the SO effects on them would complete the description of the low-energy dynamics in bulk lead, and it is done in this work.

For many years, the electron-density response of solids was studied using a free-electron gas (FEG) model in which the electron valence density is parametrized by a single quantity: the density parameter r_s, which stands for the average interelectron distance.[11] The FEG model gave insight into basic properties of the momentum- and frequency-dependent dynamical dielectric response. However, band-structure effects that are missing in a FEG model frequently can produce strong impact on the dynamical dielectric response of solids. In particular, interband transitions (not presented in a FEG model) give rise, for instance, to a strong red-shift of the Ag plasmon frequency[12] or to a negative momentum dispersion of the plasmon in Cs.[13] Moreover, these transitions can dominate in some materials the energy-loss landscape in the low-energy-transfer domain.[14–16]

In three-dimensional (3D) solids, the FEG model predicts the existence of a r_s-dependent threshold for collective excitations, exceeding in metals several eV. Hence, according to the FEG theory, plasmons can not participate directly in the low-energy dynamical processes near the Fermi surface. However, in the 1950s it was predicted[17,18] the existence of a very-low-energy excitation, which should be present in systems with several energy bands crossing the Fermi level with different Fermi velocities v_F, as it is the case of bulk Pb. This very-low-energy mode presents an acousticlike dispersion at small momentum transfers q's, i.e., $\omega_{\mathrm{AP}} = v_{\mathrm{AP}} q$, where v_{AP} is the group velocity of the acoustic plasmon

being very close to the Fermi velocity in the energy band with the slower carriers. Thus, the $\omega_{\rm AP}$ frequency tends to zero as $q \to 0$. Exchange of acoustic plasmons has been suggested as a possible mechanism of electron pairing in superconductors (see, i.e., Ref. 19 and references therein). Nevertheless, to the best of our knowledge, these kinds of acousticlike modes have not been demonstrated to exist in bulk metallic systems experimentally. A similar mode has been recently predicted[20,21] and proved experimentally[22–24] on metal surfaces. On the other hand, recent detailed *ab initio* calculations of the dynamical dielectric response in a variety of bulk metallic systems such as MgB_2,[25,26] Pd,[27] transition-metal dichalcogenides,[28,29] and CaC_6 (Ref. 16) predicted, with some initial controversy,[14,15] the existence of such kinds of acoustic plasmons in metallic systems. In particular, in the case of Pd and CaC_6, this acousticlike mode disperses in all three symmetry directions, while in the layered compounds MgB_2 and $NbSe_2$, the corresponding mode exists only for the momentum transfers along the direction perpendicular to the basal planes.

The main aim of this study is twofold. First, the complexity of the low-energy electronic response of bulk Pb is demonstrated, together with the role of different physical ingredients. Second, the results on the modes characterized by an acousticlike dispersion are presented and analyzed in detail. In particular, we demonstrate the strongly anisotropic character of such low-energy collective excitations in bulk lead. The calculations of the low-energy collective excitations have been done using the first-principles pseudopotential approach within the time-dependent density functional theory (TDDFT).[30,31]

The rest of the paper is organized as follows: In Sec. II, the details of the *ab initio* calculations of the dynamical dielectric response of 3D solids are presented. In Sec. III, the general results for bulk Pb for the low-energy regime are presented together with comparison with experimental optical data, while in Sec. IV the acousticlike collective excitations are analyzed in detail. Finally, the main conclusions are presented in Sec. V. Unless otherwise stated, atomic units are used throughout, i.e., $e^2 = \hbar = m_e = 1$.

II. CALCULATION METHOD

A key quantity in the description of dynamical dielectric response properties of solids is the dynamical structure factor $S(\mathbf{Q},\omega)$ since, within the first Born approximation, the inelastic scattering cross section at momentum transfer $\mathbf{Q}$ and energy ω of x rays and electrons is proportional to it.[11] $S(\mathbf{Q},\omega)$ is related by the fluctuation-dissipation theorem to the dielectric function $\varepsilon(\mathbf{r},\mathbf{r}',\omega)$. For a periodic solid,

$$S(\mathbf{Q},\omega) = -\frac{\Omega|\mathbf{q}+\mathbf{G}|^2}{2\pi}\mathrm{Im}\left[\varepsilon^{-1}_{\mathbf{G},\mathbf{G}}(\mathbf{q},\omega)\right], \tag{1}$$

where Ω is the normalization volume, $\mathbf{G}$ is a reciprocal-lattice vector, vector $\mathbf{q}$ is located in the Brillouin zone (BZ), $\mathbf{Q} = \mathbf{q} + \mathbf{G}$, and $\mathrm{Im}[\varepsilon^{-1}_{\mathbf{G},\mathbf{G}'}(\mathbf{q},\omega)]$ is the so-called energy-loss function, whose Fourier coefficients are related to those of the density-response function for interacting electrons $\chi(\mathbf{r},\mathbf{r}',\omega)$ through

$$\varepsilon^{-1}_{\mathbf{G},\mathbf{G}'}(\mathbf{q},\omega) = \delta_{\mathbf{G},\mathbf{G}'} + v_{\mathbf{G}}(\mathbf{q})\chi_{\mathbf{G},\mathbf{G}'}(\mathbf{q},\omega), \tag{2}$$

where $v_{\mathbf{G}}(\mathbf{q}) = \frac{4\pi}{|\mathbf{q}+\mathbf{G}|^2}$ is the Fourier transform of the bare Coulomb interaction. Note that in this definition, the $\mathbf{Q}$ vector is not restricted to be located inside the first BZ.

A crucial quantity in the evaluation of Eq. (2) is the density-response function χ, which in the framework of TDDFT (Refs. 30 and 31) satisfies the matrix equation

$$\chi_{\mathbf{G},\mathbf{G}'}(\mathbf{q},\omega) = \chi^{0}_{\mathbf{G},\mathbf{G}'}(\mathbf{q},\omega) + \sum_{\mathbf{G}''}\sum_{\mathbf{G}'''}\chi^{0}_{\mathbf{G},\mathbf{G}''}(\mathbf{q},\omega) \times \left[v_{\mathbf{G}''}(\mathbf{q})\delta_{\mathbf{G}'',\mathbf{G}'''} + K^{\rm XC}_{\mathbf{G}'',\mathbf{G}'''}(\mathbf{q})\right]\chi_{\mathbf{G}''',\mathbf{G}'}(\mathbf{q},\omega), \tag{3}$$

where $\chi^{0}_{\mathbf{G},\mathbf{G}'}(\mathbf{q},\omega)$ is the matrix of the Fourier coefficients of the density-response function for noninteracting Kohn-Sham electrons. $K^{\rm XC}_{\mathbf{G},\mathbf{G}'}(\mathbf{q})$ stands for the Fourier components of the exchange-correlation (XC) kernel, whose exact form is unknown. Thus, approximations must be used to describe $K^{\rm XC}_{\mathbf{G},\mathbf{G}'}(\mathbf{q})$. Here, we use two frequently used approaches for the description of $K^{\rm XC}$: the random-phase approximation (RPA) (here, one simply sets $K^{\rm XC}_{\rm RPA}$ to zero, i.e., neglects the short-range exchange and correlation effects) and the time-dependent local-density approximation (TDLDA).[32]

We evaluate the $\chi^{0}_{\mathbf{G},\mathbf{G}'}(\mathbf{q},\omega)$ matrix by calculating first the spectral function matrix $S^{0}_{\mathbf{G},\mathbf{G}'}(\mathbf{q},\omega)$ using the following expression:[33,34]

$$S^{0}_{\mathbf{G},\mathbf{G}'}(\mathbf{q},\omega) = \frac{1}{\Omega}\sum_{\mathbf{k}}^{\rm BZ}\sum_{n}^{\rm occ}\sum_{n'}^{\rm unocc}\langle\psi_{n\mathbf{k}}|e^{-i(\mathbf{q}+\mathbf{G})\cdot\mathbf{r}}|\psi_{n'\mathbf{k}+\mathbf{q}}\rangle\langle\psi_{n'\mathbf{k}+\mathbf{q}}| \times e^{i(\mathbf{q}+\mathbf{G}')\cdot\mathbf{r}}|\psi_{n\mathbf{k}}\rangle\delta(\varepsilon_{n\mathbf{k}} - \varepsilon_{n'\mathbf{k}+\mathbf{q}} + \omega). \tag{4}$$

In Eq. (4), n and n' are band indexes, wave vectors $\mathbf{k}$'s are in the first BZ, and $\varepsilon_{n\mathbf{k}}$ and $\psi_{n\mathbf{k}}$ are Bloch eigenvalues and eigenfunctions, respectively, of the Kohn-Sham Hamiltonian. From the knowledge of $S^{0}_{\mathbf{G},\mathbf{G}'}(\mathbf{q},\omega)$, the imaginary part of $\chi^{0}_{\mathbf{G},\mathbf{G}'}(\mathbf{q},\omega)$ is easily evaluated using the relation

$$S^{0}_{\mathbf{G},\mathbf{G}'}(\mathbf{q},\omega) = -\frac{1}{\pi}\mathrm{sgn}(\omega)\mathrm{Im}\left[\chi^{0}_{\mathbf{G},\mathbf{G}'}(\mathbf{q},\omega)\right], \tag{5}$$

where $\mathrm{sgn}(\omega) = 1$ (-1) for $\omega > 0$ $(\omega < 0)$. The real part of $\chi^{0}_{\mathbf{G},\mathbf{G}'}(\mathbf{q},\omega)$ is obtained from the corresponding imaginary part using the Hilbert transform.

Inclusion of the $\mathbf{G} \neq \mathbf{G}'$ matrix elements in Eq. (3) accounts for the so-called crystalline local-field effects (LFEs),[35] which can be significant if there is notable spatial variation in the electron density in the system. If LFEs are neglected, the energy-loss function is simply given by

$$\mathrm{Im}\left[\epsilon^{-1}_{\mathbf{G},\mathbf{G}}(\mathbf{q},\omega)\right] = \frac{\mathrm{Im}[\epsilon_{\mathbf{G},\mathbf{G}}(\mathbf{q},\omega)]}{|\epsilon_{\mathbf{G},\mathbf{G}}(\mathbf{q},\omega)|^2} = \frac{\mathrm{Im}[\epsilon_{\mathbf{G},\mathbf{G}}(\mathbf{q},\omega)]}{\{\mathrm{Re}[\epsilon_{\mathbf{G},\mathbf{G}}(\mathbf{q},\omega)]\}^2+\{\mathrm{Im}[\epsilon_{\mathbf{G},\mathbf{G}}(\mathbf{q},\omega)]\}^2}. \tag{6}$$

In this work, in the density functional theory (DFT) ground-state calculations, the electron-ion interaction is represented by a norm-conserving nonlocal pseudopotential,[36] and the local density approximation (LDA) is chosen for the exchange and correlation potential, with the use of the Perdew-Zunger[37] parametrization of the XC energy of Ceperley and Alder.[38] Well-converged results for the face-centered-cubic (fcc) bulk

Pb with the experimental lattice parameter $a = 4.95$ Å have been obtained with a kinetic energy cutoff of 14 Ry, including ∼150 plane waves in the expansion of the Bloch states.

Two different sets of calculations were carried out in evaluating Eq. (4). First, $S^0_{\mathbf{G},\mathbf{G}'}(\mathbf{q},\omega)$ was calculated in the range $0 < \omega < 30$ eV with a step of $\Delta\omega = 0.005$ eV, the band indexes in Eq. (4) running up to $n = 25$. A Monkhorst-Pack[39] $96 \times 96 \times 96$ grid of $\mathbf{k}$ vectors was used in the BZ sampling which corresponds to the inclusion of ≈9300 points in the irreducible part of the BZ (IBZ). The delta function was represented by a Gaussian of width of 0.05 eV. Second, in order to properly describe the acousticlike modes at energies below 1 eV, Eq. (4) was evaluated in the $0 < \omega < 4$ eV range, with a step $\Delta\omega =$ 1 meV and taking into account up to 12 energy bands. In this second set of calculations, a fine $432 \times 432 \times 432$ grid was used, with ≈850 000 $\mathbf{k}$ points in the IBZ, and the width of the Gaussian replacing the delta function was set to 2 meV.

In Fig. 1, the calculated band structure of bulk fcc lead along some high-symmetry directions of the first BZ is shown, with (solid lines) and without (dashed lines) inclusion of SO interaction in the Hamiltonian of the system. As the fcc lattice is centrosymmetric, due to the Kramers degeneracy,[40] each band is double degenerated in both cases. The calculated band structure is in good agreement with other calculations (see, i.e., Refs. 6 and 41) and with the experimental one[42] when the SO term is taken into account. As can be seen in Fig. 1, the inclusion of the SO interaction has sizable effects on the bands crossing the Fermi level (of p-orbital character), mainly around the high-symmetry points of the BZ. Thus, SO effects on the band structure of bulk Pb are expected to show up on the low-energy dielectric properties of this material.

The band-structure calculations were performed with inclusion of the SO term in the Hamiltonian fully self-consistently. In the evaluation of $S^0_{\mathbf{G},\mathbf{G}'}(\mathbf{q},\omega)$, the SO coupling enters Eq. (4) through the energy spectrum (via the δ function) and coupling matrices (the brackets). We checked that the replacement of the spinor wave functions by scalar ones in the evaluation of χ^o slightly modifies the calculated dielectric properties of Pb in comparison with the full SO results, however, without important changes.

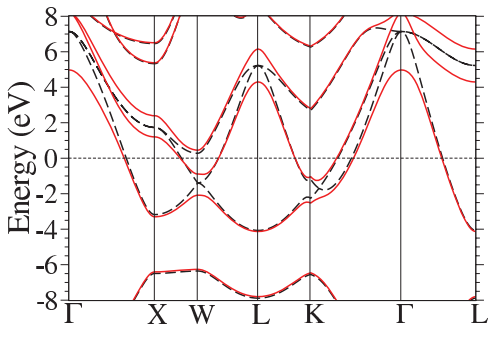

FIG. 1. (Color online) Band structure of bulk lead, calculated with (solid lines) and without (dashed lines) spin-orbit coupling term in the Hamiltonian. The horizontal dashed line represents the Fermi level set to zero.

III. GENERAL RESULTS

In the FEG model, the plasma frequency is determined as $\omega_p = \sqrt{4\pi n/m^*}$ with n being the average electron density and m^* the electron effective mass, which in terms of the density parameter r_s reads as $\omega_p = \sqrt{3/r_s^3\, m^*}$. For lead, using the value of $r_s = 2.298$ determined on base of experimental data, one obtains $\omega_p^{\mathrm{FEG}} = 13.53$ eV. This value is in good agreement with the one obtained in electron energy-loss experiments (see, e.g., Ref. 43 and references therein). Thus, the energy-transfer range $\omega \leqslant 8$ eV, which is of interest here, is well below the bulk plasmon energy in lead. Note also that by calculating the dielectric response up to 30 eV, the present results are well converged with respect to the finite-energy range used in the numerical Hilbert transform procedure.

Comparison of the calculated energy-loss function with optical experimental data from Ref. 44 obtained at 140 K and room temperature is performed in Fig. 2. The calculated curves correspond to the smallest momentum transfer $Q = 0.014$ a.u. along the Γ–X direction, allowing comparison with optical measurements. As can be seen in the figure, the loss function calculated without the spin-orbit interaction significantly deviates from both experimental curves. In particular, the first peak in the calculated curve is located at 1.5 eV, i.e., at a notably lower energy in comparison with experiment. Other broad peaks centered at energies of 2.35 and 3.4 eV are also located at lower energies. Only inclusion of the SO coupling in the band structure leads to a fairly good agreement in the energy positions of all three features in this energy range with the experimental ones, especially with the measurements

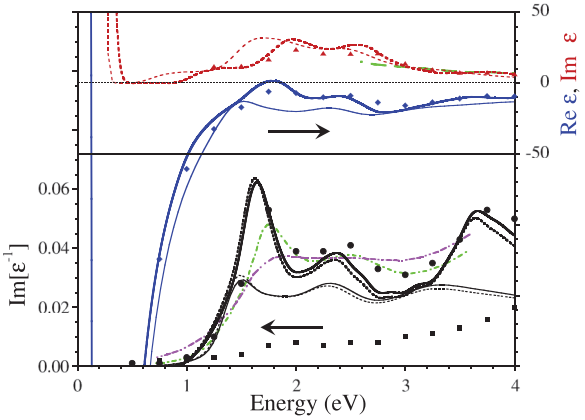

FIG. 2. (Color online) (Upper panel) Imaginary (dashed lines) and real (solid lines) parts of the dielectric function obtained in the RPA calculations at $Q = 0.014$ a.u. along the Γ–X direction. In the lower panel, the corresponding energy-loss function evaluated with (solid lines) and without (dotted lines) inclusion of the LFEs is shown. Thick (thin) lines present results obtained with (without) inclusion of spin-orbit splittings. Experimental data for the loss function from Ref. 44 measured at 140 K and room temperature are shown by thin dashed-dotted and dashed-dashed-dotted-dotted lines, respectively. Thick long-dashed line in the upper panel shows the measured imaginary part of the dielectric function (Ref. 46). Filled triangles, diamonds, and circles present corresponding data obtained in first-principles calculations of Glantschnig and Ambrosch-Draxl (Refs. 9 and 45). Filled squares show the loss function obtained in the REELS experiment (Ref. 45).

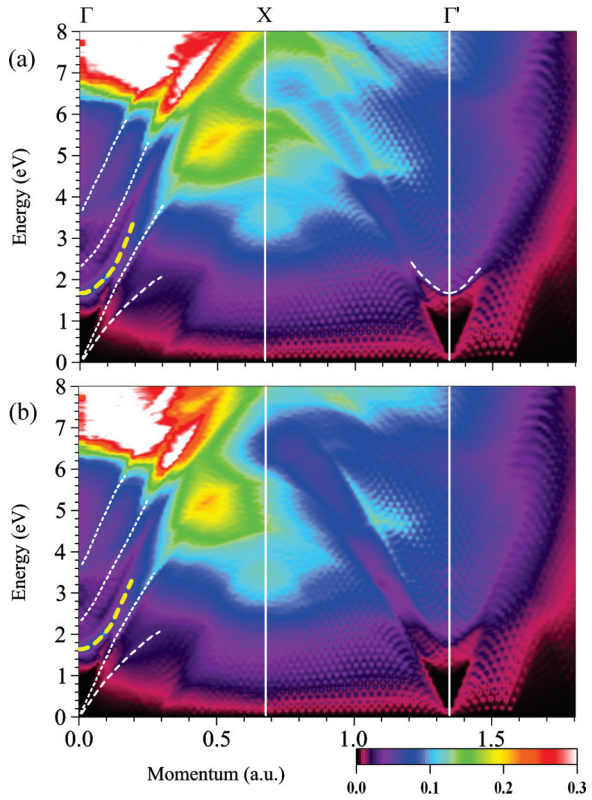

FIG. 3. (Color online) Calculated energy-loss function of Pb versus energy ω and momentum transfer Q along the Γ–X symmetry direction. Results are obtained with inclusion of the SO coupling and the RPA kernel and (a) with and (b) without inclusion of the LFEs. Thick yellow dashed lines highlight dispersion of the plasmon modes. Thin white dashed lines show peaks corresponding to strongly damped modes, while the thin dotted ones highlight the modes which strongly disperse upwards up to energies $\omega \gtrsim 4$ eV. Vertical white lines mark positions of the X point and the Γ point in the subsequent BZ.

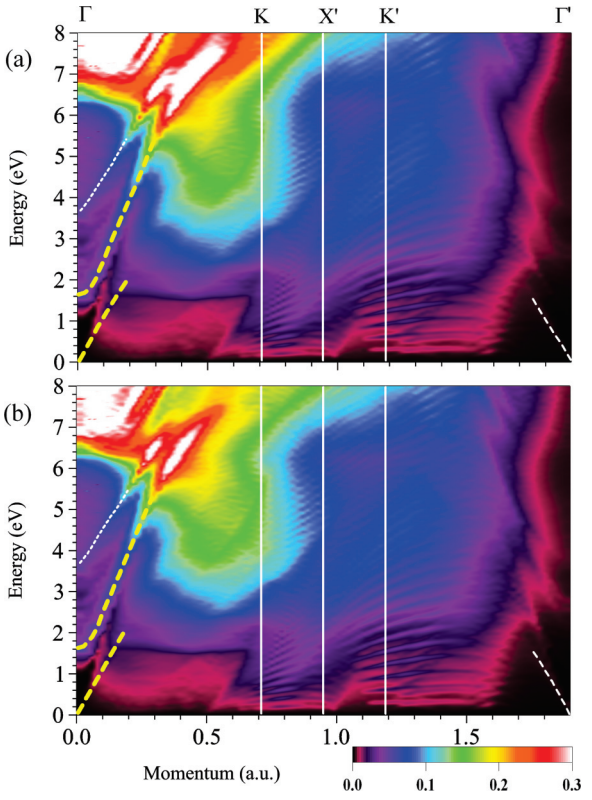

FIG. 4. (Color online) Calculated energy-loss function of Pb versus energy ω and momentum transfer Q along the Γ–K symmetry direction. Results are obtained with inclusion of the SO coupling and the RPA kernel and (a) with and (b) without inclusion of the LFEs. Thick yellow dashed lines highlight dispersion of the plasmon modes. Thin white dashed lines show peaks corresponding to strongly damped modes, while the thin dotted one highlights an interband mode dispersing upwards until it enters the manifold of s–p transitions. Vertical white lines mark positions of the K point and the X, K, and Γ points in the subsequent BZs.

carried out at 140 K. Also, our data with the SO interaction included are in good agreement with *ab initio* calculations of Ref. 9. Some quantitative differences observed between two *ab initio* results are at the level of uncertainty in such kinds of calculations.

In Figs. 3–5, the energy-loss function, $\mathrm{Im}[\varepsilon^{-1}(\mathbf{Q},\omega)]$, calculated using the RPA approximation for the exchange-correlation kernel and including the SO interaction, is presented as a function of the energy transfer ω and value of the momentum transfer $\mathbf{Q}$ along three high-symmetry directions, both including and neglecting the LFEs. In these figures, at small Q's one can observe several peaks in the energy range below the prominent broad peak structure presented at energies above ∼6.5 eV, which coincides with the energy threshold for interband transitions between the occupied s states (those located at energies below −6 eV in Fig. 1) and the p states above the Fermi level.

The strong increase of intensity of the interband peak at ∼1.65 eV in the calculated loss function with the SO coupling included can be explained by the fact that, as seen in the upper panel of Fig. 2, the real part of the dielectric function reaches zero at a close energy due to a sharp increase in the corresponding imaginary part of the dielectric function. It seems in our calculations this effect is more pronounced than in the calculation of Glantsching and Ambrosch-Draxl.[9] Nevertheless, the evaluated loss functions in both calculations are rather similar in this energy range. Only little differences can be observed at larger energies, where the loss function calculated in Ref. 9 is slightly larger than that evaluated in this work. This is explained by the larger imaginary part of the dielectric function in our calculation in the 1.7–2.7 eV energy region and the lower real part at energies above 2 eV. From this analysis we can conclude that the experimental optical data reflect clear SO effects. Note that in the experimental data of Ref. 44, the two first lowest-energy peaks are barely visible in the room-temperature loss spectra and significantly more pronounced in the measurements performed at $T = 140$ K. This is in agreement with the fact that Pb presents a strong electron-phonon coupling, which modifies the one-electron energy levels with increasing temperature. Hence, one can expect that in measurements performed at even lower temperatures, the first interband peak might increase its intensity and downshift in energy, in such a way improving agreement with the calculations.

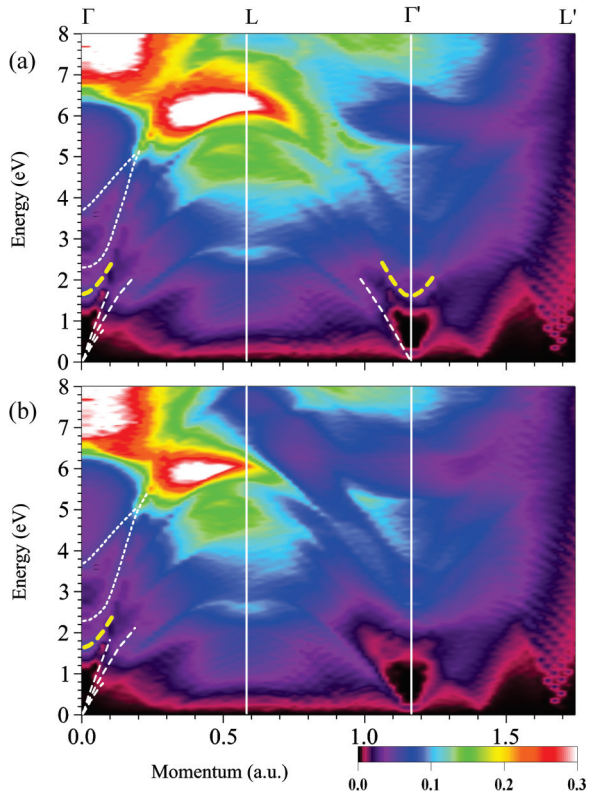

FIG. 5. (Color online) Calculated energy-loss function of Pb versus energy ω and momentum transfer Q along the Γ–L symmetry direction. Results are obtained with inclusion of the SO coupling and the RPA kernel and (a) with and (b) without inclusion of the LFEs. Thick yellow dashed lines highlight dispersion of the plasmon modes. Thin white dashed lines show peaks corresponding to strongly damped modes, while the thin dotted ones highlight two interband modes dispersing upwards until they merge each other. Vertical white lines mark positions of the L point and the Γ and L points in the subsequent BZs.

On the other hand, comparison of the calculated results with the recently measured data obtained by reflection electron energy-loss spectroscopy[45] (REELS) reveals only a broad weak peak around 2 eV and presents significant underestimation in intensity of the whole spectrum. These might be a consequence that this REELS experiment setup might have insufficient resolution in this low-energy range, being apparently more suitable at higher energies.[45]

In Figs. 3–5 one can see how the peaks in the loss function strongly disperse upward upon increase of momentum-transfer values in all three directions. Thus, the dominating 1.65-eV peak increases its energy up to ∼3.5 eV (∼8 eV) at $Q =$ 0.2 (0.6) a.u. along the Γ–X (Γ–K) direction. On the other hand, the 1.65-eV peak possesses along the Γ–L direction much less dispersion and quickly disappears at $\omega = 2.3$ eV. The other weaker 2.35- and 3.7-eV peaks disperse upward in Γ–X and Γ–K up to energies above 6 eV where they enter the manifold corresponding to s-p interband transitions and can be resolved as separate features up to $\omega = 8$ eV. On the contrary, along Γ–L these upper-energy peaks disperse up to energy of ∼5.2 eV where they merge each other and a much stronger peak continues dispersion up to energies about 6.3 eV. Starting from $Q = 0.6$ a.u., the dispersion of this peak turns from positive to negative and it can be clearly resolved up to $Q \sim 1$ a.u.

In the following we present a systematic analysis of the effect of the main physical ingredients such as LFEs, SO coupling, and XC effects on the low-energy collective electronic excitations in bulk Pb.

A. Local-field effects

From comparison of the upper and lower panels in Figs. 3–5 one can deduce that the LFEs affect the calculated dielectric properties rather weakly. From Figs. 2 and 6, it is seen that this effect is barely visible at small momentum transfers. Along the Γ–X, Γ–K, and Γ–L directions, the main result of the LFEs in the formation of the excitation spectra in Pb consists in some distortion of the intensity of the aforementioned peaks at

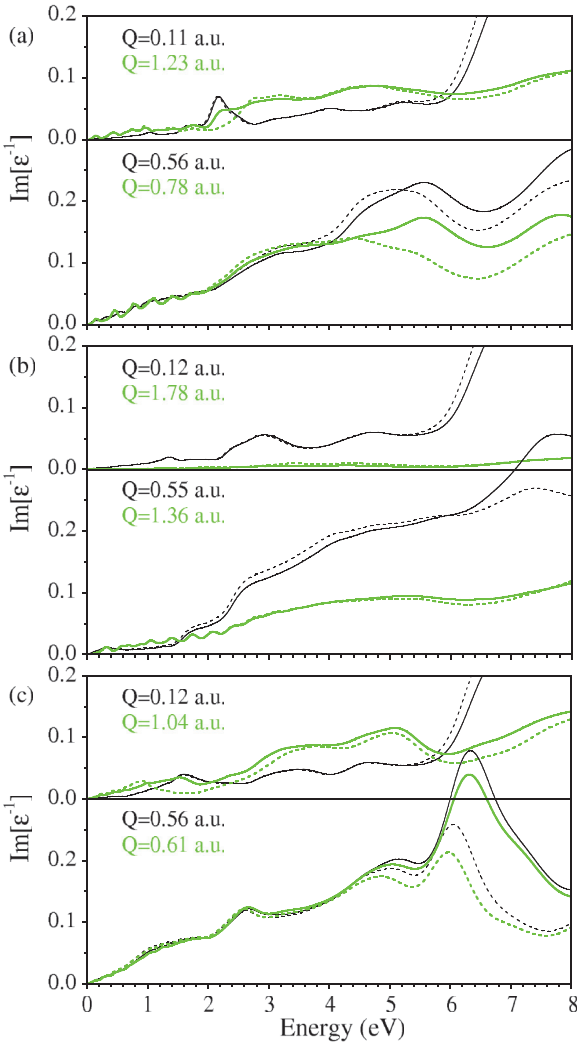

FIG. 6. (Color online) Calculated energy-loss function at some fixed momentum transfers Q's as a function of energy. Calculations are performed with inclusion of the SO interaction at the RPA level. Solid (dashed) lines are obtained with (without) inclusion of LFEs. Thick (thin) lines stand for the greater (smaller) Q reported in each panel. The data at **Q**'s along Γ–X, Γ–K, and Γ–L symmetry directions are presented in (a), (b), and (c), respectively.

the finite-momentum transfers. At energies above $\omega \sim 6$ eV, the LFEs produce significant increases in intensity of the dominant peaks.

Additionally, the LFEs produce an upward shift in energy of all the features. However, the effect is not very pronounced and in general does not exceed several tenths of eV. Thus, in Fig. 6 one can see that the major upward shift about 0.3–0.4 eV occurs in the case of the ∼6-eV feature at intermediate momentum transfers along the Γ–L direction.

Another consequence of the inclusion of the LFEs is transmission of the 1.65-eV peak at small Q's to momentum transfers close to $Q = 2\pi/a = 1.35$ a.u. in the Γ–X direction. At momentum transfers close to this Q one can see how the intensity of the loss function at $\omega \approx 1.65$ eV notably increases when the LFEs are included. At $Q = 1.23$ a.u., the corresponding increase in the loss function at $\omega \approx 2.25$ eV due to LFEs can be seen in Fig. 6(a). Also, some increase in the loss function caused by the LFEs due to the $\omega = 1.65$ eV mode can be detected in the vicinity of $Q = 1.16$ a.u. along the Γ–L direction. The example of this enhancement can be seen in Fig. 6(c), where a broad feature in the loss function appears at energies around 1.6 eV at $Q = 1.04$ a.u. when the LFEs are taken into account. However, in general, the impact of the LFEs on the loss spectra in Pb, being noticeable at certain energies, is not so strong as in other systems such as MgB_2 (Ref. 25) and compressed lithium.[47] This signals about less inhomogeneity in the valence charge density in Pb in comparison with those systems.

B. XC kernel

In Fig. 7, the calculated energy-loss function for several values of **Q** belonging to the three different high-symmetry directions is plotted, where comparison between results obtained with the RPA and the TDLDA kernels is made. As can be seen in the figure, the main effect of the TDLDA with respect to the RPA is the increase of the intensity of the calculated $\mathrm{Im}[\varepsilon^{-1}(\mathbf{Q},\omega)]$, but without qualitative changes in its shape. The most significant change is seen in Fig. 7(c) where the dominant interband peak in the Γ–L direction is shifted downward in energy by ∼0.1 eV upon inclusion of the XC effects at the TDLDA level.

C. SO-interaction-induced effects

Inclusion of the SO coupling also affects the dielectric response of bulk Pb in an anisotropic way. As shown in Fig. 8, in all three high-symmetry directions the SO interaction increases the intensity of the broad feature located at energies above 6 eV. As was previously discussed, inclusion of the SO in the calculation of the energy-loss function has sizable effects at small-momentum transfers at energies of 1.65, 2.35, and 3.7 eV. The impact of the SO coupling on the excitation spectra can also be observed in Fig. 8. Thus, at $Q = 0.11$ a.u. along Γ–X the appearance of a clear peak at 2.15 eV and two broad peaks at $\omega = 4.0$ and 5.2 eV caused by the SO interaction can be appreciated. At larger Q's, the effect is smaller and consists mainly in the upward shift of the existing peaks. The same trend is observed in the Γ–K and Γ–L directions as well, although with less impact at intermediate and large-momentum transfers. Additionally, in Fig. 8 one can detect that at small Q's in the low-energy region the inclusion of the SO interaction leads to the appearance of a pronounced peak. Thus, at $Q = 0.11$ a.u. along the Γ–X direction it is located at $\omega = 1$ eV, whereas at $Q = 0.12$ a.u., the corresponding peak presents at $\omega = 1.15$ and 1.6 eV along the Γ–K and Γ–L directions, respectively. The dispersion of these peaks is highlighted by dashed lines in Figs. 3–5 and it is discussed in the next section.

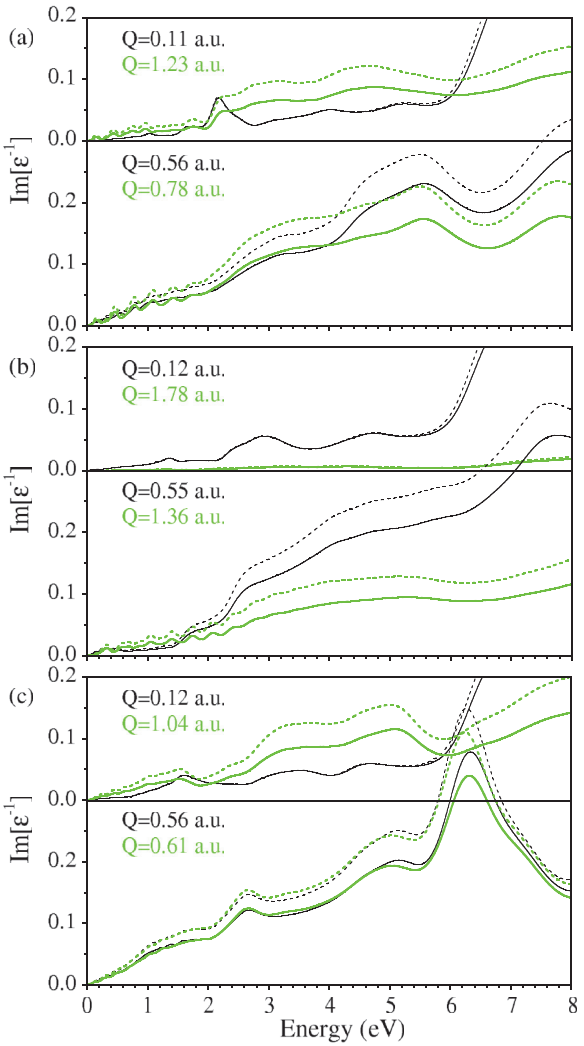

FIG. 7. (Color online) Solid lines represent the same as in Fig. 6, while the dashed lines show the energy-loss function evaluated at corresponding **Q**'s with inclusion of XC effects at the TDLDA level. Thick (thin) lines stand for the greater (smaller) Q reported in each panel.

IV. ACOUSTICLIKE EXCITATIONS

In the "low-momentum–low-energy" region of Figs. 3–5 the calculated loss function presents several peaks dispersing almost linearly with momentum, whose energy is vanishing upon vanishing of the momentum transfer. Upon momentum-transfer increase, these peaks can be traced up to an energy of about 2 eV in Γ–K and Γ–L, and up to even higher energies in Γ–X. The number of such peaks depends on

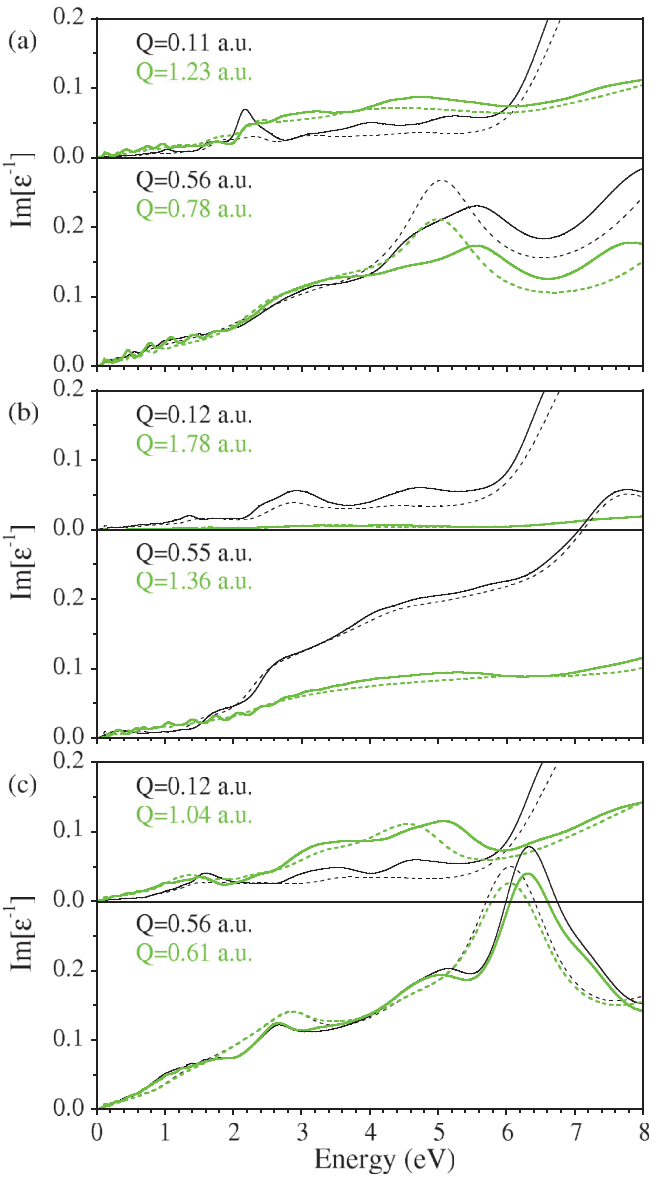

FIG. 8. (Color online) Solid lines represent the same as in Fig. 6, while the dashed lines show the energy-loss function evaluated at corresponding **Q**'s at the RPA level without inclusion of the SO interaction. Thick (thin) lines stand for the greater (smaller) Q reported in each panel.

the direction, being two in the case of Γ–X, one in Γ–K, and three along Γ–L. To study in more detail the origin of these modes characterized by an acousticlike dispersion, in Figs. 9–11 we report the calculated dielectric and energy-loss functions at almost the same small momentum transfers in all three high-symmetry directions. Here, we show the results obtained at the scalar-relativistic level and with inclusion of the SO coupling and spinor representation for wave functions. For comparison, in these figures the featureless curves derived from the Lindhard dielectric function[48] for the same q's are presented as well. The *ab initio* curves were obtained with inclusion of the LFE and the TDLDA kernel, even though these two physical ingredients were found

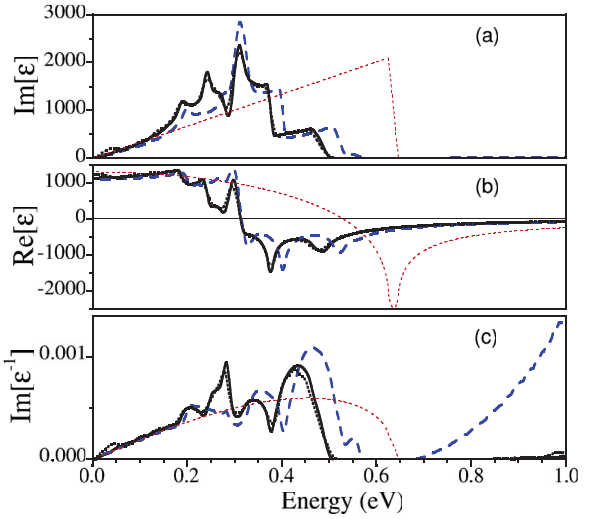

FIG. 9. (Color online) Calculated (a) imaginary and (b) real parts of the dielectric function and (c) energy-loss function evaluated at $q \simeq 0.028$ a.u. along the Γ–X direction. Thick dashed, dotted, and solid lines correspond to the results obtained at the scalar-relativistic level, with inclusion of the SO coupling and scalar representation for wave functions, with inclusion of the SO coupling and spinor representation for wave functions, respectively. Thin dotted line shows corresponding quantities obtained with the Lindhard dielectric function for $r_s^{\mathrm{Pb}} = 2.298$. *Ab initio* results are obtained with inclusion of the LFE and TDLDA kernel.

to affect negligibly the results in this low-energy range in all cases.

In Fig. 9, one can observe two clear peaks in the loss function, whose shape and intensity depends on whether the SO interaction is included or excluded from the calculation, whereas the spinor representation for the wave functions has minor impact on the results as was suggested in Ref. 4. Note that we observe a similar little impact on the dielectric properties of Pb of the spinor representation for the wave functions in other symmetry directions as well. From the analysis of the real part of the dielectric function we conclude that neither of these

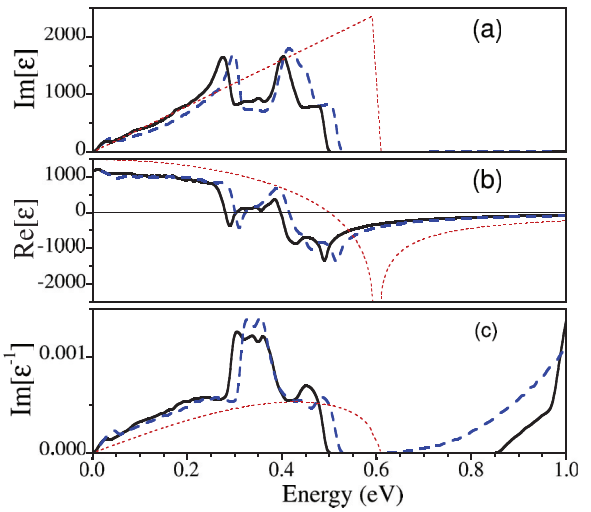

FIG. 10. (Color online) The same as in Fig. 9 evaluated at $q = 0.026$ a.u. along the high-symmetry Γ–K direction.

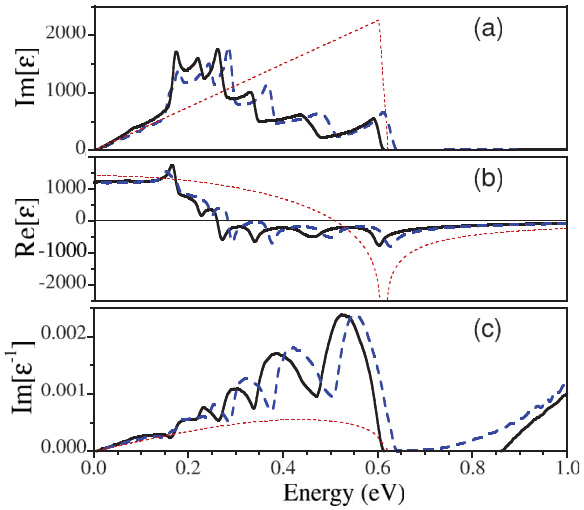

FIG. 11. (Color online) The same as in Fig. 9 evaluated at $q = 0.027$ a.u. along the high-symmetry Γ–L direction.

peaks can be considered as a true plasmon mode as the real part of ε does not cross zero at the corresponding energies. The only zero crossing in Re[ε] occurs at 0.32 eV close to the energy where Im[ε] has a maximum. As a result, at this energy the loss function presents a local minimum. Therefore, this zero crossing must be considered as a conventional Landau-overdamped mode which can not be realized.[11] At the same time, inspection of Fig. 9 shows that the peaks presented in the energy-loss function are located at energies where the Im[ε] possesses local minima. Hence, despite rather large values of the Re[ε] at corresponding energies, these peaks can be considered as corresponding to heavily damped acoustic plasmons. One can compare these results with those derived in the FEG model, where a zero crossing of Re[ε] does not produce any peak in the loss function due to the presence of a peak in Im[ε] at the close energy.

The existence of peaks in the loss function is explained by the presence of a number of peaks in Im[ε]. These peaks in Im[ε] are due to intraband excitations within the energy bands crossing the Fermi level. Although all these bands are of the same p-like character, their dispersion with different Fermi-velocity components in this symmetry direction is reflected in the presence of several peaks in Im[ε].

Concerning the Γ–K direction, the loss function presented in Fig. 10 shows a broad main peak which is centered at $\sim$0.33 eV when the SO coupling is included in the calculations. Moreover, one can see that Re[ε] is rather small at that energy and even crosses zero at 0.30 eV with positive slope, when SO is included in the calculations. This signals that this peak corresponds to a true plasmon mode, although severely damped due to decay into electron-hole pairs. The appearance of this peak in Im[ε^{-1}] can be explained by the presence of two clear main peaks in Im[ε] at 0.26 and 0.40 eV, again when the SO interaction is included in the calculations. This makes the real part of the dielectric function to cross zero three times, the second one with positive slope leading to the appearance of the peak in the loss function. Again, as it is in the Γ–X direction, in the scalar-relativistic case all the peaks in Im[ε] and Im[ε^{-1}] are located at higher energies.

At momentum transfers along the Γ–L direction, the number of peaks in the loss function is maximal. As an example, in Fig. 11 one can detect up to three clear peaks in Im[ε^{-1}] at energies of 0.30, 0.38, and 0.53 eV. Their dispersion is shown in Fig. 5. The presence of such a large number of peaks in Im[ε^{-1}] can be again explained by a large number of peaks in Im[ε] seen in Fig. 11 (up to five). However, neither of these peaks leads to an additional zero crossing in Re[ε]. For this reason, all these peaks in the loss function can be considered as being heavily damped plasmonic modes. Similar to what occurs in other symmetry directions, the effect of inclusion of SO coupling is limited to the downward shift of these modes without qualitative changes.

In the calculation at the scalar-relativistic level, we obtain that the upper border for the intraband electron-hole transitions is located at higher energies than when the SO interaction is included. This is explained by modifications in the energy bands around the Fermi surface. The main effect of the inclusion of the SO is the flattening of the band dispersion accompanying the opening energy gaps seen in Fig. 1. Consequently, this causes modifications of intraband excitations reflected in the integrated form through Eq. (4) in Im[ε]. Regarding the shape of the acousticlike dispersing modes, the SO coupling only slightly affects ε at $\mathbf{q}$'s in Γ–X, where it gives rise to a new peak (which is located at $\omega \simeq 0.27$ eV in Fig. 9).

A. Group velocities: Comparison with v_F

Concerning the group velocities v_g of the acoustic modes, the values are dependent on the momentum-transfer direction as readily seen from the slopes of the corresponding lines in Figs. 3–5, thus showing anisotropy as a result of band-structure effects. More precisely, the group velocities v_g present values of 0.33 and 0.41 a.u. in the Γ–X direction, 0.41 a.u. in Γ–K, and 0.40, 0.51, and 0.71 a.u. in Γ–L. The velocity atomic unit is 2.1877×10^6 m/s. All the reported velocities are lower than the Fermi velocity derived from the FEG model[49] of $v_F^{\mathrm{FEG}} = 0.84$ a.u. On the other hand, all the estimated v_g are higher than the experimental value of $v_F^{\mathrm{expt}} = 0.23$ a.u. (Ref. 50) obtained in skin depth measurements. Note the estimated group velocities of the acoustic modes can not be simply assigned to the Fermi velocities of the bands crossing the Fermi surface on a fixed reciprocal space point in the calculated band structure. As an example, comparison of the above reported values of v_g with the maximal Fermi velocities of the bands in the high-symmetry directions (see Fig. 1) of 0.60 a.u. (Γ–X), 0.47 and 0.54 a.u. (Γ–K), and 0.84 a.u. (Γ–L) shows clear deviations between the calculated v_F and v_g values. In all cases, $v_F > v_g$. This is as expected since collective electronic excitations can not be built faster than the velocity of the individual electrons. Thus, in each $\mathbf{q}$ direction, the maximum v_F can be seen as the upper bound for the group velocities of the acoustic modes.

B. Possibility of detection in EELS experiments

In order to evaluate the possibility of experimental detection of the aforementioned acousticlike modes, in Fig. 12 a comparison is given of the energy-loss function for the acoustic dispersing peaks at the same momentum transfers reported in

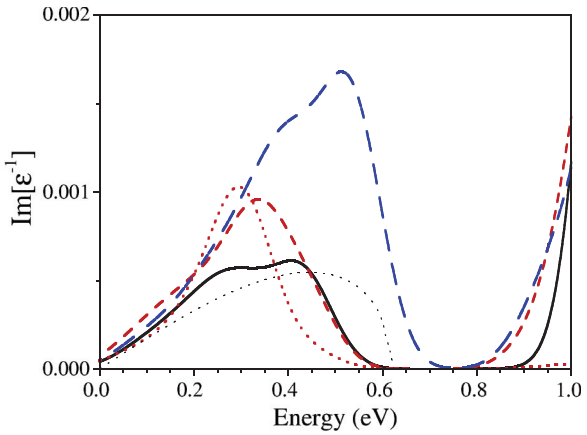

FIG. 12. (Color online) Comparison of the energy-loss function for the acousticlike dispersing peaks in all three high-symmetry directions at the same momentum transfers as in Figs. 9–11. Thick solid, dashed, and long-dashed lines show results at q's along the Γ–X, Γ–K, and Γ–L symmetry directions, respectively. Thick dotted line is the loss function evaluated at momentum transfer corresponding to vector q in the second BZ along Γ–K. Loss function derived from the Lindhard dielectric function at $q = 0.027$ a.u. is presented by the thin dotted line. First-principles results are broadened with a broadening parameter of 75 meV (see text).

Figs. 9–11 in all three high-symmetry directions, together with the loss function derived from the Lindhard dielectric function at $q = 0.027$ a.u. Also, the acousticlike plasmon mode is shown for $\mathbf{q}$ in the second BZ in the Γ–K direction by a dashed red line. A Gaussian broadening has been applied to the first-principles results. The broadening parameter was fixed as 75 meV, corresponding to the experimentally measured linewidth of quantum-well states in Pb(111) thin films[51] at $T = 5$ K. The intensity of the acoustic mode peak is maximal in the Γ–L direction. However, from Fig. 12 we conclude that the most suitable acoustic plasmon for experimental detection corresponds to the peak dispersing in the second BZ in the Γ–K direction. It presents the smaller linewidth once the broadening is applied, and more importantly it is located in a (q,ω) range in which the energy-loss function presents vanishing values except for the acoustic mode itself, getting isolated in this way (see Fig. 12). Note also that the cross section probed in EELS experiments is proportional to q^2,[52] making weak features in the low-momentum-transfer range more difficult to be resolved.

However, an additional possibility of detecting an acoustic plasmon in bulk Pb can be suggested based on the general results obtained for the momentum transfer along the Γ–X direction. As seen from Fig. 3, the fastest dispersing acoustic mode reaches an energy of $\sim$5 eV at $q \simeq 0.45$ a.u., with a gradual increase of its intensity. Thus, once the peak at $\sim$5 eV and $q \simeq 0.45$ a.u. is detected, one could trace its dispersion back towards vanishing energy- and momentum-transfer values.

V. CONCLUSIONS

We have presented first-principles calculations of the low-energy ($\omega \leqslant 8$ eV) collective electronic excitations in bulk Pb and studied in detail the effect of the main physical ingredients involved, as well as the existence and character of acousticlike modes. Good agreement with available optical experimental data[44] is interpreted as an evidence of remarkable SO effects, also in agreement with other theoretical works.[9,45]

In general, strong anisotropic effects are found, resulting in a distinct topology of $\mathrm{Im}[\varepsilon^{-1}_{\mathbf{G},\mathbf{G}}(\mathbf{q},\omega)]$ for $\mathbf{q} \in \Gamma$–K. The LFE and the SO coupling have sizable effects on the dielectric screening of bulk Pb, showing an anisotropic behavior. For $\mathbf{q}$ vectors in the second BZ, the impact of the LFE on the energy-loss function is remarkable. Inclusion of exchange-correlation effects through the TDLDA kernel increases the intensity of the energy-loss function in the studied range, however, without affecting its shape in a significant way.

Very-low-energy modes with acousticlike dispersions are found in all three studied high-symmetry directions and are shown to be a consequence of band-structure effects. The character of these acoustic modes depends on the direction of $\mathbf{q}$. The experimental detection of these acoustic modes by electron energy-loss measurements seems feasible as these modes keep their character up to $\omega \simeq 2$ eV, and can reach energies as high as 5 eV in the Γ–X direction.

ACKNOWLEDGMENTS

We acknowledge financial support from the Spanish MICINN (Grant No. FIS2010-19609-C02-01), the Departamento de Educación del Gobierno Vasco, and the University of the Basque Country (Grant No. GIC07-IT-366-07).

[1] E. V. Chulkov, A. G. Borisov, J. P. Gauyacq, D. Sánchez-Portal, V. M. Silkin, V. P. Zhukov, and P. M. Echenique, Chem. Rev. (Washington, D. C.) **106**, 4160 (2006).
[2] P. M. Echenique, R. Berndt, E. V. Chulkov, Th. Fauster, A. Goldmann, and U. Höfer, Surf. Sci. Rep. **52**, 219 (2004).
[3] X. Gonze, J.-P. Michenaud, and J.-P. Vigneron, Phys. Rev. B **41**, 11827 (1990).
[4] X. Zubizarreta, V. M. Silkin, and E. V. Chulkov, Phys. Rev. B **84**, 115144 (2011).
[5] S. V. Eremeev, I. A. Nechaev, Yu. M. Koroteev, P. M. Echenique, and E. V. Chulkov, Phys. Rev. Lett. **108**, 246802 (2012).
[6] R. Heid, K.-P. Bohnen, I. Yu. Sklyadneva, and E. V. Chulkov, Phys. Rev. B **81**, 174527 (2010).
[7] L. E. Díaz-Sánchez, A. H. Romero, and X. Gonze, Phys. Rev. B **76**, 104302 (2007).
[8] I. Yu. Sklyadneva, R. Heid, K.-P. Bohnen, V. Chis, V. A. Volodin, K. A. Kokh, O. E. Tereshchenko, P. M. Echenique, and E. V. Chulkov, Phys. Rev. B **86**, 094302 (2012).
[9] K. Glantschnig and C. Ambrosch-Draxl, New J. Phys. **12**, 103048 (2010).
[10] R. C. Dynes and J. M. Rowell, Phys. Rev. B **11**, 1884 (1975).
[11] D. Pines and P. Nozières, *The Theory of Quantum Liquids* (Benjamin, New York, 1966).

[12]M. A. Cazalilla, J. S. Dolado, A. Rubio, and P. M. Echenique, Phys. Rev. B **61**, 8033 (2000).
[13]F. Aryasetiawan and K. Karlsson, Phys. Rev. Lett. **73**, 1679 (1994).
[14]V. P. Zhukov, V. M. Silkin, E. V. Chulkov, and P. M. Echenique, Phys. Rev. B **64**, 180507(R) (2001).
[15]W. Ku, W. E. Pickett, R. T. Scalettar, and A. G. Eguiluz, Phys. Rev. Lett. **88**, 057001 (2002).
[16]J. P. Echeverry, E. V. Chulkov, P. M. Echenique, and V. M. Silkin, Phys. Rev. B **85**, 205135 (2012).
[17]D. Pines, Can. J. Phys. **34**, 1379 (1956).
[18]P. Nozières and D. Pines, Phys. Rev. **109**, 1062 (1958).
[19]Y. Ishii and J. Ruvalds, Phys. Rev. B **48**, 3455 (1993).
[20]V. M. Silkin, A. García-Lekue, J. M. Pitarke, E. V. Chulkov, E. Zaremba, and P. M. Echenique, Europhys. Lett. **66**, 260 (2004).
[21]V. M. Silkin, J. M. Pitarke, E. V. Chulkov, and P. M. Echenique, Phys. Rev. B **72**, 115435 (2005).
[22]B. Diaconescu, K. Pohl, L. Vattuone, L. Savio, P. Hofmann, V. M. Silkin, J. M. Pitarke, E. V. Chulkov, P. M. Echenique, D. Farías, and M. Rocca, Nature (London) **448**, 57 (2007).
[23]S. J. Park and R. E. Palmer, Phys. Rev. Lett. **105**, 016801 (2010).
[24]K. Pohl, B. Diaconescu, G. Vercelli, L. Vattuone, V. M. Silkin, E. V. Chulkov, P. M. Echenique, and M. Rocca, Europhys. Lett. **90**, 57006 (2010).
[25]V. M. Silkin, A. Balassis, P. M. Echenique, and E. V. Chulkov, Phys. Rev. B **80**, 054521 (2009).
[26]A. Balassis, E. V. Chulkov, P. M. Echenique, and V. M. Silkin, Phys. Rev. B **78**, 224502 (2008).
[27]V. M. Silkin, I. P. Chernov, Yu. M. Koroteev, and E. V. Chulkov, Phys. Rev. B **80**, 245114 (2009).
[28]M. N. Faraggi, A. Arnau, and V. M. Silkin, Phys. Rev. B **86**, 035115 (2012).
[29]P. Cudazzo, M. Gatti, and A. Rubio, Phys. Rev. B **86**, 075121 (2012).
[30]E. Runge and E. K. U. Gross, Phys. Rev. Lett. **52**, 997 (1984).
[31]M. Petersilka, U. J. Gossmann, and E. K. U. Gross, Phys. Rev. Lett. **76**, 1212 (1996).
[32]E. K. U. Gross, J. F. Dobson, and M. Petersilka, in *Density Functional Theory II*, edited by R. F. Nalewajski (Springer, Berlin, 1996).
[33]F. Aryasetiawan and O. Gunnarsson, Phys. Rev. B **49**, 16214 (1994).
[34]F. Aryasetiawan, in *Strong Coulomb Correlations in Electronic Structure Calculations*, edited by V. I. Anisimov (Gordon and Beach, Singapore, 2001).
[35]S. L. Adler, Phys. Rev. **126**, 413 (1962).
[36]G. B. Bachelet, D. R. Hamann, and M. Schlüter, Phys. Rev. B **26**, 4199 (1982).
[37]J. P. Perdew and A. Zunger, Phys. Rev. B **23**, 5048 (1981).
[38]D. M. Ceperley and B. J. Alder, Phys. Rev. Lett. **45**, 566 (1980).
[39]H. J. Monkhorst and J. D. Pack, Phys. Rev. B **13**, 5188 (1976).
[40]M. Tinkam, *Group Theory and Quantum Mechanics* (McGraw-Hill, New York, 1971).
[41]M. J. Verstraete, M. Torrent, F. Jollet, G. Zérah, and X. Gonze, Phys. Rev. B **78**, 045119 (2008).
[42]G. Jézéquel and I. Pollini, Phys. Rev. B **41**, 1327 (1990).
[43]A. M. Ashton and G. W. Green, J. Phys. F: Met. Phys. **3**, 179 (1973).
[44]A. G. Mathewson and H. P. Myers, Phys. Scr. **4**, 291 (1971).
[45]W. S. M. Werner, K. Glantschnig, and C. Ambrosch-Draxl, J. Phys. Chem. Ref. Data **38**, 1013 (2009).
[46]J. C. Lemonnier, M. Priol, and S. Robin, Phys. Rev. B **8**, 5452 (1973).
[47]I. Errea, A. Rodriguez-Prieto, B. Rousseau, V. M. Silkin, and A. Bergara, Phys. Rev. B **81**, 205105 (2010).
[48]G. Grosso and G. P. Parravicini, *Solid State Physics* (Academic, San Diego, 2000).
[49]N. W. Ashcroft and N. D. Mermin, *Solid State Physics* (Thomson Learning, Southbank, Victoria, 1976).
[50]J. Bardeen and J. R. Schrieffer, in *Progress in Low Temperature Physics*, edited by C. J. Groter (Interscience, New York, 1961).
[51]I. Po Hong, C. Brun, F. Patthey, I. Y. Sklyadneva, X. Zubizarreta, R. Heid, V. M. Silkin, P. M. Echenique, K. P. Bohnen, E. V. Chulkov, and W.-D. Schneider, Phys. Rev. B **80**, 081409(R) (2009).
[52]H. Kuzmany, *Solid-State Spectroscopy. An Introduction* (Springer, Berlin, 1998).